



The Acoustic Emission Characteristics of Sandstone With Cyclic Loading and Acid-Base Corrosion Coupling

Yu Yang, Shunyi Wang*

School of Civil Engineering, Liaoning Technical University, Fuxin 123000, China

*Corresponding author Email: 499338901@qq.com

Abstract. Rocks may undergo changes in internal structural integrity due to the coupling of cyclic loading and acidbase corrosion (CL-AC), which can subsequently alter their mechanical properties. Based on uniaxial compression tests with acoustic emission, the coupling of CL-AC on the mechanical behavior of sandstone and the evolution of acoustic emission characteristics were investigated. The results indicated that as the coupling of CL-AC increased, the uniaxial compressive strength of sandstone decreased significantly. The cumulative acoustic emission count and energy of the pre-treated sandstone showed a decreasing trend. The proportion of low-frequency acoustic emission signals from the sandstone increased, while the proportions of mid and high-frequency signals decreased. That is, the coupling of CL-AC facilitated the formation of larger cracks. As the sandstone approached failure, low-frequency, high-amplitude and mid-frequency, high-amplitude acoustic emission signals disappeared, which may serve as a precursor to sandstone failure. The *RA-AF* value distribution of the sandstone showed that the pre-treated sandstone primarily exhibited tensile cracks, while the lossless sandstone was dominated by shear cracks. That is, the coupling of CL-AC promoted the propagation of tensile cracks and inhibited the expansion of shear cracks. These findings offered valuable insights into the damage and failure mechanisms of sandstone under the coupling of CL-AC, providing crucial guidance for the prevention of rock dynamic hazards.

Keywords: Mechanical property, Acoustic emission, Cyclic loading, Acid-base corrosion.

1 Introduction

The Liaoning province of China was rich in abundant and high-quality coal reserves. However, prolonged mining activities had gradually depleted surface and shallow coal deposits, resulting in an increasing shift toward the extraction of deeper coal resources. The geological conditions for deep mining had become progressively more complex, leading to a gradual increase in mining risks^[1-2] Especially after mining ceased, the abandoned goaf experienced stress disturbances from the adjacent working face, leading to significant cyclic loading and unloading effects. This process induced fatigue damage to the roof strata of the old goaf, further promoting the development of internal

fractures and resulting in a marked decline in the rock's mechanical properties^[3-5]. Simultaneously, after mining ceased and dewatering was stopped, the old goaf gradually filled with water during the groundwater recharge process, forming a water accumulation zone. The water-rock interaction eroded the surrounding rock, further degrading the mechanical properties of the rock mass^[6-8]. Under the coupling of cyclic loading and acid-base corrosion (CL-AC), the ultimate bearing capacity of the rock mass was significantly weakened. When the ultimate bearing capacity of the old goaf roof fell below the self-weight load, instability occurred, leading to further collapse of the goaf. This, in turn, triggered secondary disasters, such as rock bursts, mine tremors, and surface subsidence^[9]. Therefore, investigating the changes in mechanical behavior and the damage evolution patterns of the roof rock layers in abandoned goaf, under the coupling of CL-AC, was crucial for ensuring the safety of mining operations and the long-term stability of the mine.

During the deformation and failure of rocks, stress waves were generated, resulting in the emission of acoustic signals. The characteristics of the acoustic emission reflected the changes in the rock mass's damage state under loading, serve as precursors to failure, and indicate the progression of crack propagation^[10]. The characteristics of acoustic emission ring-down counts and energy variations, together with the stress-strain curve, can be used to delineate the stages of the damage process^[11]. In recent years, the use of acoustic emission *b*-value, real-time amplitude-frequency characteristics, and entropy values had shown distinct advantages in early warning of rock failure, particularly in predicting rock bursts and dynamic disasters. The overall decline of the *b*-value, the generation of high-amplitude low-frequency signals, and the emergence of V-shaped entropy characteristics served as precursors to rock failure^[12-13]. Many scholars had proposed a novel crack classification method based on the acoustic emission parameters *RA-AF*, and its reliability had been validated through experiment^[14]. By analyzing the variations in acoustic emission waveform characteristics, the crack features and distribution within the rock can be identified^[15-16].

Based on real-time acoustic emission monitoring, this paper investigated the mechanical behavior and the evolution of acoustic emission characteristics of sandstone under the coupling of CL-AC. The sandstone was pre-treated with multiple cycles of loading and unloading, as well as varying levels of acid-base corrosion, before undergoing uniaxial compression testing. Subsequently, a systematic analysis was conducted on parameters such as acoustic emission count, energy, peak frequency, and amplitude. The crack evolution and failure modes of sandstone were examined based on the distribution of *RA-AF* values. This paper explored the changes in the mechanical behavior and damage evolution characteristics of sandstone under the coupling of CL-AC. It provided valuable insights into the damage and failure mechanisms of roof strata in old mining areas, contributing to the prevention of rock dynamic hazards.

2 Materials and Methods

2.1 Materials

The fine sandstone samples used in this experiment were collected from a dynamic pressure mining roadway approximately 1,000 meters below ground in the Liaoning province of China. The sandstone had a gray-white appearance, with a fine-grained structure and homogeneous texture. After collecting the rock samples on-site, they were sealed and transported to the laboratory. In accordance with the standards set by the International Society for Rock Mechanics (*ISRM*), the samples were cored, cut, and polished into standard cylindrical specimens with a diameter of 50 mm and a height of 100 mm, ensuring that the end faces were parallel within ± 0.02 mm. To minimize the impact of sample variability on the experiment, specimens with visible defects were discarded. Specimens exhibiting significant deviations in apparent density, longitudinal wave velocity, or unstable waveforms were then removed. The average apparent density of the sandstone specimens was 2.405 g/cm^3 , and the average longitudinal wave velocity was $2,495 \text{ m/s}$. The remaining qualifying specimens, some of which were shown in Figure 1, were selected as the subjects for this study.

The mineral composition of the rock samples, determined by XRD analysis, was shown in Figure 2. It consisted of quartz (49.2%), lagioclase (30.4%), potassium feldspar (11.4%), chlorite (4.2%), illite (3.8%), and talc (1.0%).

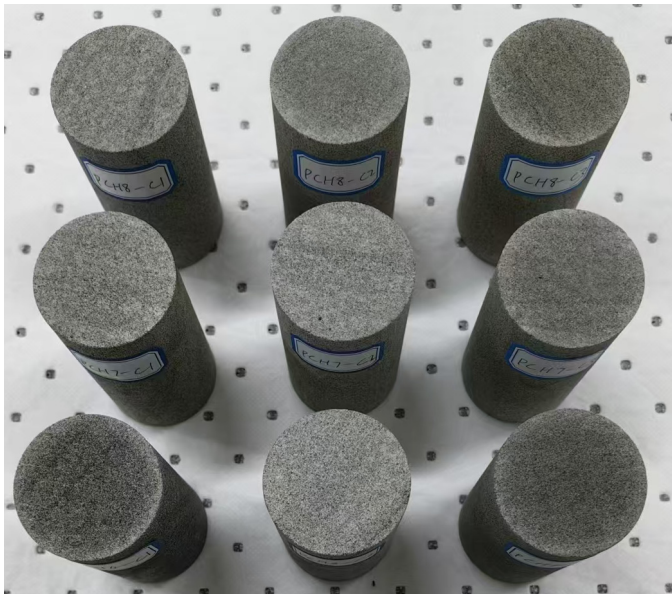


Fig. 1. Photographs of select rock samples.

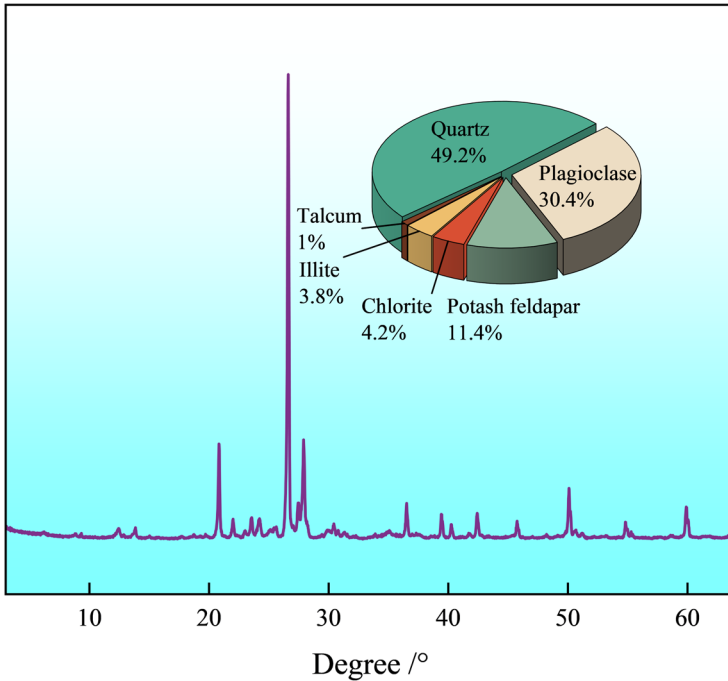


Fig. 2. XRD analysis results of the sandstone.

2.2 Pre-treatment of Sandstone Samples

2.2.1 Cyclic loading and unloading treatment. Uniaxial cyclic loading and unloading tests were conducted to simulate the mechanical damage induced by dynamic pressure disturbances from adjacent working faces in old mining areas, preparing rock samples with varying degrees of damage. The lower stress loading limit (σ_{\min}) was set at 15 MPa (approximately 19% of σ_c), while the upper stress loading limits (σ_{\max}) were set at 25 MPa (approximately 32% of σ_c), 35 MPa (approximately 45% of σ_c), and 45 MPa (approximately 58% of σ_c). Fifteen sandstone specimens were equally divided into three groups, labeled PA, PB, and PC. The loading method employed in the experiment was stress control, while the loading procedure was as follows: Initially, the specimens were loaded at a rate of $v_1=0.5$ kN/s until reaching the lower stress limit (σ_{\min}), where they were maintained for 180 seconds. Subsequently, the specimens were loaded at a rate of $v_2=1.0$ kN/s until reaching the upper stress limit (σ_{\max}). Upon reaching this limit, the specimens were immediately unloaded at the same rate (v_2) to the lower stress limit (σ_{\min}) and held for 30 seconds. This cycle constituted one loading/unloading cycle, repeated until 50 cycles were completed. Finally, the specimens were unloaded at a rate of v_1 to 0. The experimental procedure and apparatus are illustrated in Figure 3.

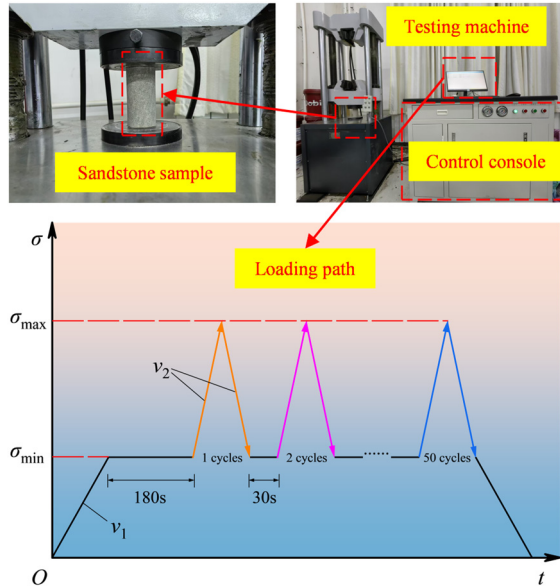


Fig. 3. Preparation of sandstone samples under cyclic loading conditions.

2.2.2 Acid-base corrosion treatment. The abandoned mining area gradually transformed into a waterlogged region due to groundwater infiltration, which had further weakened the strength of the surrounding rock mass. Acid-base corrosion tests were conducted on the rock samples that had undergone cyclic loading and unloading. Mine water typically has a complex composition, with variations in pH and different ionic constituents. To investigate the effect of mine water with varying pH levels on the mechanical properties of sandstone, solutions with pH values of 4, 5, 6, 7, and 8 were prepared, along with a saline solution at a fixed ratio (mineralization of 1 g/L). The specimens in each group were labeled H4, H5, H6, H7, and H8, Respectively (Figure 4).



Fig. 4. Process of acid-base corrosion treatment.

2.3 Uniaxial Compression Test Monitored by Acoustic Emission Monitoring

Real-time acoustic emission monitoring was conducted throughout the loading process using the AMSY-6 acoustic emission tester (Figure 5). Four acoustic emission sensors were placed on opposite sides of the sandstone specimen, at distances of 20 mm and 80 mm from the top. A coupling agent was applied to the contact surfaces between the specimen and the sensors to ensure optimal contact. The acoustic emission sensors converted elastic waves into electrical signals, which were then amplified by the preamplifier. The threshold for detecting acoustic emission signals was set to 34 dB, with a signal detection frequency of 1 MHz. At the start of the experiment, two operators simultaneously pressed the mechanical loading and acoustic emission monitoring acquisition buttons to ensure data consistency.



Fig. 5. Acoustic emission monitoring equipment.

3 Acoustic Emission Characterization

3.1 Acoustic Emission Count and Energy

3.1.1 Acoustic emission count. Figure 6 illustrated the relationship between stress and strain of the rock sample under uniaxial compression. Due to the similar trend of the test results, only the samples numbered PAH7 and PCH4 were selected for analysis. The acoustic emission ringing count was significantly higher during the mid and late loading stages compared to the early loading stage. These periods experienced more crack propagation events, whereas the early loading stage was characterized by relatively stable crack closure, resulting in a lower acoustic emission ringing count. As loading time progressed, the cumulative acoustic emission ringing count followed a trend of “slow increase → rapid escalation”.

As the initial degree of damage in sandstone under the coupling of CL-AC increased, the cumulative ringing count of the rock sample gradually decreased. The reason was that as the initial fractures within the sandstone developed further, leading to decrease in the number of new fractures forming during the loading process. Consequently, the cumulative acoustic emission ringing count at the peak stress point also decreased.

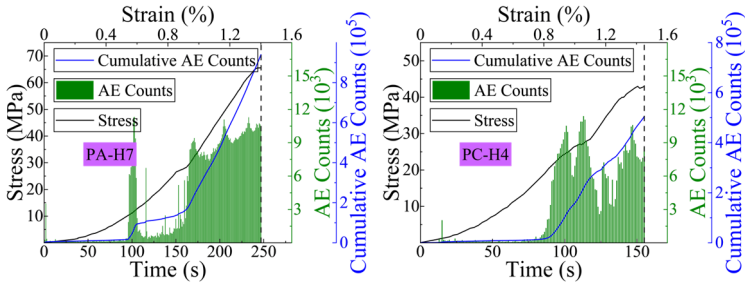


Fig. 6. The relationship between the ringing count of rock samples under different pre-treatment conditions and time, stress, and strain.

3.1.2 Acoustic emission energy. The relationship between the acoustic emission energy and loading time of the rock sample during the uniaxial compression test is presented in Figure 7.

The variation in cumulative acoustic emission energy of the rock sample after the coupling of CL-AC can be divided into three stages, exhibiting a trend of “gradual increase → stepwise development → rapid surge”. The acoustic emission energy during the early and mid-loading stages was relatively low, as the cracks remained closed or were in the process of gradual formation, resulting in minimal acoustic emission activity. In contrast, the late loading stage exhibited significantly higher acoustic emission energy, signaling the onset of failure with numerous high-energy acoustic emission events due to the extensive propagation of secondary fractures within the sandstone.

As the coupling of CL-AC intensified, the cumulative acoustic emission energy of the rock sample gradually decreased. Because the weakening of the sandstone’s integrity and cementation reduced the stored elastic energy, resulting in a corresponding decline in acoustic emission energy.

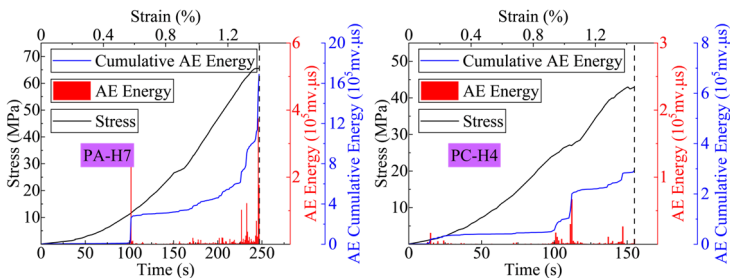


Fig. 7. The relationship between acoustic emission energy, time, stress, and strain under different preprocessing conditions.

3.2 Analysis of the Acoustic Emission Frequency-Amplitude Characteristics

The frequency of acoustic emission correlated with crack size. Generally, high-frequency acoustic emission signals corresponded to the smaller cracks, while low-frequency signals were associated with the larger cracks.

As shown in Figure 8, the acoustic emission frequency range was divided into four phases: low-frequency (0-50kHz), mid-frequency (50-125kHz), high-frequency (125-225kHz), and ultra-high frequency (225-350kHz). It was evident that the acoustic emission signals from the rock sample were primarily concentrated in the low-frequency and mid-frequency phase, while low-frequency acoustic emission signals occurred less than mid-frequency acoustic emission signals significantly. This indicated that the expansion of large cracks continued throughout the loading stage, but the number of the large cracks was limited. The high-frequency phase was concentrated in the mid-loading stage, indicating that small cracks primarily developed during this stage. The ultra-high frequency phase exhibited a sporadic distribution with no distinct characteristics. As the specimen approached failure, high and ultra-high frequency acoustic emission signals ceased, while mid and low-frequency signals diminished but persisted. This indicated that the development of small cracks within the sandstone had ceased, while the propagation of a few large cracks took precedence.

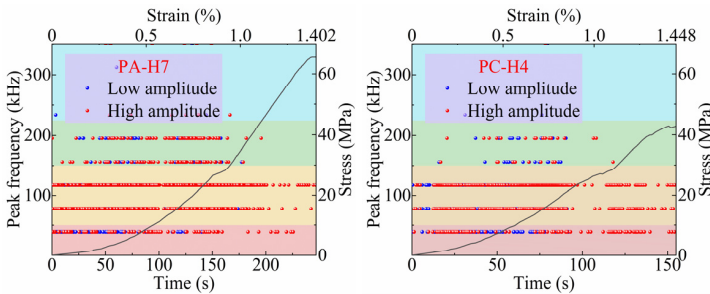


Fig. 8. The variations in peak frequency and amplitude of the rock samples.

Table 1. Percentage of different frequency acoustic emission signals¹.

Labels	Low-frequency(%)	Mid-frequency(%)	High-frequency(%)	Ultra-high frequency(%)
PA-H4	11.73	84.53	3.64	0.10
PA-H5	6.96	88.29	4.62	0.13
PA-H6	6.14	88.16	5.48	0.22
PA-H7	5.40	87.83	6.32	0.46
PA-H8	6.09	89.06	4.74	0.11

¹In this experiment, The acoustic emission frequency range was divided into four phases: low-frequency (0-50kHz), mid-frequency (50-125kHz), high-frequency (125-225kHz), and ultra-high frequency (225-350kHz).

PB-H4	15.26	81.69	3.01	0.05
PB-H5	12.10	83.62	4.11	0.17
PB-H6	9.70	85.09	5.08	0.13
PB-H7	9.17	85.70	4.87	0.26
PB-H8	10.25	84.34	5.11	0.30
PC-H4	24.61	72.19	3.17	0.03
PC-H5	11.55	84.94	3.37	0.14
PC-H6	12.93	85.83	1.19	0.06
PC-H7	9.41	86.37	3.66	0.56
PC-H8	12.82	82.79	4.18	0.21

The distribution of crack sizes in sandstone can be quantitatively analyzed by the proportion of peak frequencies in different frequency phases, as shown in Table 1. The table showed that as the upper stress limit of cyclic loading and unloading increased, coupled with the intensification of acid-base corrosion, the proportion of low-frequency signals gradually rose, while the proportions of mid and high-frequency signals decreased. That is, the increase in the initial damage to the sandstone, the likelihood of forming larger cracks within the specimen also increased. The greater the initial damage, the more developed the initial fractures and defects within the sandstone, which significantly increased the potential for the formation of larger cracks during loading.

An analysis of the acoustic emission amplitude was presented in Figure 8. Based on the median amplitude of each rock sample's acoustic emission, the signals were classified into low and high amplitude categories. The acoustic emission amplitudes of the rock samples ranged from 34 to 100 dB, with median amplitudes between 40 and 43 dB. This indicated that the majority of the acoustic emission signals had relatively low amplitudes, suggesting that the number of large cracks formed in the rock samples during loading was much smaller than that of smaller cracks. During the loading process, low amplitude signals from the sandstone were primarily distributed in the early and mid-stages, with few or no signals in the later stages. In contrast, high-amplitude signals were observed throughout the entire loading process.

An analysis of the combined frequency-amplitude characteristics of the acoustic emission signals revealed that, just before failure, the rock sample exhibited only low and mid-frequency, high-amplitude signals. Therefore, these frequency-amplitude characteristics can be served as precursors to rock failure.

3.3 Analysis of RA-AF Distribution and Evolution of Crack Types

3.3.1 RA-AF distribution analysis. The processed acoustic emission signals effectively captured the evolution of microcracks during the rock failure process. Previous studies had classified microcrack types according to the analysis of the RA-AF acoustic emission parameters. The RA value represents the ratio of rise time to the maximum amplitude of the acoustic emission signal, while the AF value is the ratio of the ringing count to the duration of the acoustic emission. The calculation principles were illustrated in Figure 9.

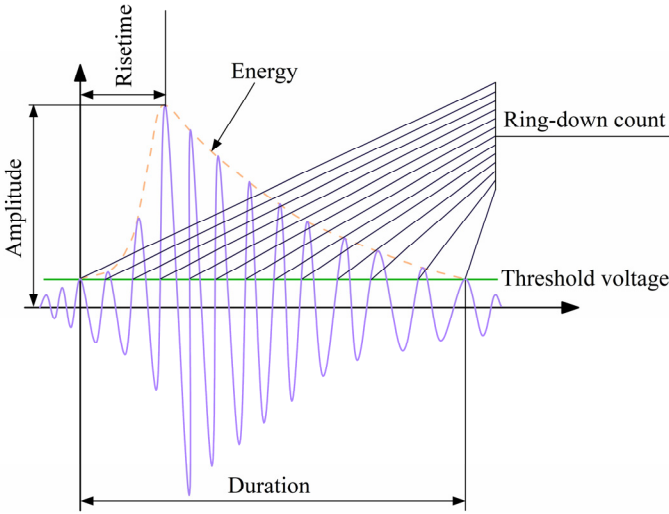


Fig. 9. Calculation principle of RA-AF.

$$RA = RT/V \tag{1}$$

$$AF = C/DT \tag{2}$$

Where RT is the rise time. V is the maximum amplitude of the acoustic emission signal corresponding to the voltage. C is the ringing count of acoustic emission exceeding the threshold value. DT is the duration of the impact. The relationship between voltage and acoustic emission amplitude is as follow:

$$A = 20 \times \lg(V/1\mu V) \tag{3}$$

In the experiment, the main amplifier is set to 40 dB, with an additional 40 dB pre-amplifier connected. Simplifying the equation based on this setup yields the following:

$$V = 10^{(A/20+1)} mV \tag{4}$$

During the loading process of rocks, various types of internal cracks were generated, which can be primarily categorized into three types: tensile cracks, shear cracks, and tensile-shear combined cracks. The distinct differences in acoustic emission characteristics can be used to distinguish between crack types. By analyzing the proportion of each crack type, the primary failure modes of the rock can be quantitatively distinguished. When the acoustic emission signal exhibited a low RA value and a high AF value (i.e., $AF/RA > K$), it indicated rapid energy release and the development of tensile cracks. Whereas, high RA values and low AF values (i.e., $AF/RA < K$) corresponded to shear crack propagation and the slower energy release. K represented the slope of the boundary between the tensile and shear regions, with a value of 300 in this experiment.

The relationship between $RA-AF$ distribution and crack types at the peak load point for rock samples with different initial damage levels were illustrated in Figure 10. As shown in the figure below, the acoustic emission signal characteristics of the pretreated rock samples predominantly exhibited $AF/RA > K$, indicating that tensile cracks were more developed within the sandstone, with tensile failure being the primary failure mode.

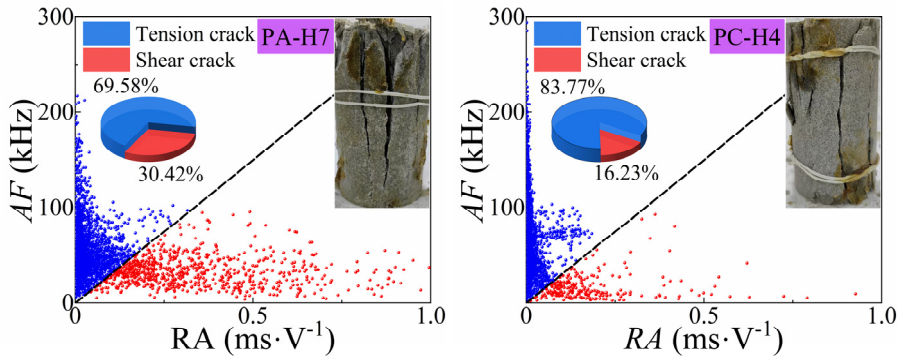


Fig. 10. The distribution of $RA-AF$ values for rock samples.

3.3.2 Analysis of crack evolution patterns in sandstone. To gain a deeper understanding of the crack evolution patterns in sandstone during uniaxial compression, an analysis was conducted on the changes in tensile and shear cracks in the rock samples throughout the loading process. Since the crack evolution trends of the pretreated rock samples were similar, only the pretreated samples PC-H4 and PA-H7 were analyzed, as shown in Figure 11. During the loading process, the variation trends of tensile and shear cracks in all rock samples were similar, following a pattern of “slow growth → rapid development → slow growth”.

Crack growth was restricted during the compaction and plastic stages. During the compaction stage, tensile cracks were more prevalent in the sandstone, indicating that at lower loading levels, the development of tensile cracks predominated. During the plastic stage, the rock samples continued to propagate along pre-existing cracks, forming macroscopic fractures, with very few new cracks being generated. The elastic stage was the primary phase of crack development in sandstone, with the majority of crack growth occurring during this stage. The types of cracks that develop during this phase determined the material’s primary failure mode. During the elastic stage, the number of tensile cracks in the pretreated rock samples consistently exceeded that of shear cracks, leading to a failure mode dominated by tensile failure.

The macroscopic failure modes of the sandstone showed that the acoustic emission parameters $RA-AF$ effectively reflected crack evolution during the loading process, as well as the dominant failure mode.

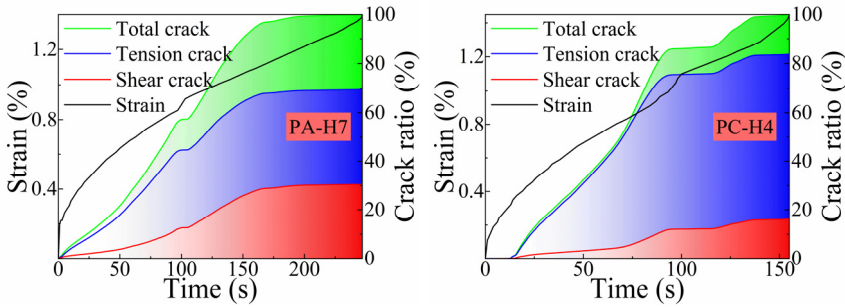


Fig. 11. The distribution patterns of tensile and shear cracks in rock samples.

4 Discussion

This study examined the mechanical behavior and damage mechanisms of fine sandstone under the coupling of CL-AC. The results of the uniaxial compression tests indicated that sandstone subjected to cyclic loading and acid-base corrosion exhibited significant differences in peak strength. This was because cyclic loading induced repeated tension and shear in the intergranular cementing materials, resulting in a gradual increase in the number and size of internal cracks, which weakened the mechanical properties of the sandstone. Additionally, during the acid-base corrosion process, the internal substances were dissolved and mineral composition was changed by chemical solution, modifying the microstructure of the sandstone, further weakening its mechanical properties.

Simultaneously, the acoustic emission characteristics of sandstone during uniaxial compression were investigated, including acoustic emission counts and energy, peak frequency and amplitude, and the distribution of *RA-AF* values. The changes in acoustic emission counts and energy provided an objective reflection of the development of internal cracks and damage evolution within the sandstone. The acoustic emission frequency and amplitude further characterized the crack size distribution and damage state. The *RA-AF* distribution reflected the evolution of crack types and failure modes in the sandstone. Taken together, the above acoustic emission parameters reflected the coupling of CL-AC on the damage, crack evolution, and fracture characteristics of sandstone during the loading process. As the coupling of CL-AC intensified, the proportion of large cracks gradually increased, while the degree of damage becomes more severe. Additionally, the disappearance of low-amplitude, high-frequency signals during uniaxial compression can be served as an effective indicator for predicting rock failure.

This paper has practical significance for predicting the stability of sandstone roof strata under the coupling of CL-AC. By monitoring characteristic changes in acoustic emission signals, the safety factor in engineering can be improved, enabling early detection and prevention of mining accidents. Future studies should consider increasing the number of cyclic loading and unloading cycles to better align with real-world engineering conditions. By establishing a damage variable and a constitutive model based

on acoustic emission parameters, the damage process of rocks can be quantitatively described. Given the strong correlation between rock acoustic emission parameters and the damage state, crack propagation, and failure modes in underground tunnels, onsite microseismic monitoring (*SOS*) is recommended for coal mine tunnels.

5 Conclusion

This study examined the coupling of CL-AC on the mechanical behavior and acoustic emission evolution of sandstone through acoustic emission monitoring. The uniaxial compression test results revealed changes in the mechanical properties of sandstone, while the analysis of acoustic emission parameters provided a theoretical basis for understanding damage evolution. The main conclusions were as follows:

(1) In the uniaxial compression test, the acoustic emission count followed a “gradual increase → apid development” trend, while the acoustic emission energy exhibited a “gradual increase → stepwise development → sharp increase” pattern. Overall, the cumulative acoustic emission count and energy of pretreated sandstone decreased as the coupling of CL-AC intensified.

(2) As the coupling of CL-AC intensified, the frequency of acoustic emission signals in sandstone shifted, with a higher proportion of low-frequency signals. This indicated that the coupling of CL-AC romoted the growth of larger cracks. Regarding the amplitude-frequency characteristics of the acoustic emission, it is observed that, near failure, low-frequency high-amplitude and mid-frequency highamplitude signals disappeared. This characteristic may serve as a precursor to the failure of sandstone.

(3) The distribution of *RA-AF* values in sandstone revealed that pretreated sandstone predominantly exhibited tensile cracks under uniaxial compression, which accounted for over 70% of the total crack count. This suggested that the coupling of CL-AC promoted the expansion of tensile cracks while inhibiting the growth of shear cracks.

Abbreviations

CL-AC: the coupling of cyclic loading and acidbase corrosion

References

1. Xia, D. & Zhang, L. Coupling coordination degree between coal production reduction and CO₂ emission reduction in coal industry. *Energy*. 258, 124902 (2022).
2. Çelik, A. & Özçelik, Y. Investigation of the effect of caving height on the efficiency of the longwall top coal caving production method applied in inclined and thick coal seams by physical modeling. *Int. J. Rock Mech. Min. Sci.* 162, 105304 (2023).
3. Bagde, M.N. & Petroš, V. Fatigue properties of intact sandstone samples subjected to dynamic uniaxial cyclical loading. *Int. J. Rock Mech. Min. Sci.* 42, 237-250 (2005).
4. Liu, E.L. & He, S.M. Effects of cyclic dynamic loading on the mechanical properties of intact rock samples under confining pressure conditions. *Eng. Geol.* 125, 81-91 (2012).

5. Tan, T.J., Wang, E.Y., Wang, X.R., Ma, L.Z. & Yao, W.L. Resistivity and damage of coal under cyclic loading and unloading. *Eng. Geol.* 323, 107234 (2023).
6. Feng, X.T. & Ding, W.X. Experimental study of limestone micro-fracturing under a coupled stress, fluid flow and changing chemical environment. *Int. J. Rock Mech. Min. Sci.* 44, 437-448 (2007).
7. Cao, Q.Y., Yang, L., Qian, Y.H. & Zhao, Z.X. Spatial distribution characteristics of coal mine drainage water quality in China. *Mine Water. Environ.* 41, 1096-1105 (2022).
8. Chen, W. et al. Aging deterioration of mechanical properties on coal-rock combinations considering hydro-chemical corrosion. *Energy.* 282, 128770 (2023).
9. Poulsen, B.A. et al. Strength reduction on saturation of coal and coal measures rocks with implications for coal pillar strength. *Int. J. Rock Mech. Min. Sci.* 71, 41-52 (2014).
10. Zhang, D.M., Zhu, S.D., Zhou, M.L., Huang, H.W. & Tong, Y. Damage quantification and failure prediction of rock: A novel approach based on energy evolution obtained from infrared radiation and acoustic emission. *Int. J. Rock Mech. Min. Sci.* 183, 105920 (2024).
11. Wang, J., Li, J.T., Shi, Z.M. & Chen, J.C. Fatigue damage and fracture evolution characteristics of sandstone under multistage intermittent cyclic loading. *Theor. Appl. Fract. Mech.* 119, 103375 (2022).
12. Zhao, K. et al. Evaluation of internal microcrack evolution in red sandstone based on time-frequency domain characteristics of acoustic emission signals. *Constr. Build. Mater.* 260, 120435 (2020).
13. Xie, N., Tang, H.M., Yang, J.B. & Jiang, Q.H. Damage evolution in dry and saturated brittle sandstone revealed by acoustic characterization under uniaxial compression. *Rock Mech. Rock Eng.* 55, 1303-1324 (2022).
14. Zhao, Y.G., Li, X.B., Huang, L.Q., Zhang, Z.C. & Xu, Z.H. Characteristic stress variation and microcrack evolution of granite subjected to uniaxial compression using acoustic emission methods. *J. Rock Mech. Geotech. Eng.* 16, 3511-3523 (2024).
15. Du, K., Li, X.F., Tao, M. & Wang, S.F. Experimental study on acoustic emission (AE) characteristics and crack classification during rock fracture in several basic lab tests. *Int. J. Rock Mech. Min. Sci.* 133, 104411 (2020).
16. Liu, J.F. et al. Acoustic emission evolution and fracture mechanism of rock for direct tensile failure. *Int. J. Rock Mech. Min. Sci.* 185, 105974 (2025).

Open Access This chapter is licensed under the terms of the Creative Commons Attribution-NonCommercial 4.0 International License (<http://creativecommons.org/licenses/by-nc/4.0/>), which permits any noncommercial use, sharing, adaptation, distribution and reproduction in any medium or format, as long as you give appropriate credit to the original author(s) and the source, provide a link to the Creative Commons license and indicate if changes were made.

The images or other third party material in this chapter are included in the chapter's Creative Commons license, unless indicated otherwise in a credit line to the material. If material is not included in the chapter's Creative Commons license and your intended use is not permitted by statutory regulation or exceeds the permitted use, you will need to obtain permission directly from the copyright holder.

